Supporting Information: Theoretical Insights into Ultrafast-Decaying and Long-Lived States of ortho-Nitrophenol upon Photoexcitation in the Gas Phase

Satoi Wada,[†] Takuro Tsutsumi,[†] Kenichiro Saita,[†] Taro Sekikawa,[‡] and Tetsuya Taketsugu[*,†,¶]

†*Department of Chemistry, Faculty of Science, Hokkaido University, Sapporo 060-0810, Japan*

‡*Department of Applied Physics, Faculty of Engineering, Hokkaido University, Sapporo 060-8628, Japan*

¶*Institute for Chemical Reaction Design and Discovery (WPI-ICReDD), Hokkaido University, Sapporo 001-0021, Japan*

E-mail: take@sci.hokudai.ac.jp.

Contents

1 Absorption spectrum

Absorption spectrum was calculated at the MRSF-TDDFT level of theory. The experimental absorption spectrum of *o*-NP in the gas phase, reported by Ernst *et al.*, exhibits three peaks at approximately 207, 259, and 331 nm.[4] **Figure S1** shows the calculated absorption spectrum, where the peak positions are blue-shifted compared to the experimental spectrum. However, the overall trend in peak positions remains consistent with the experimental data.

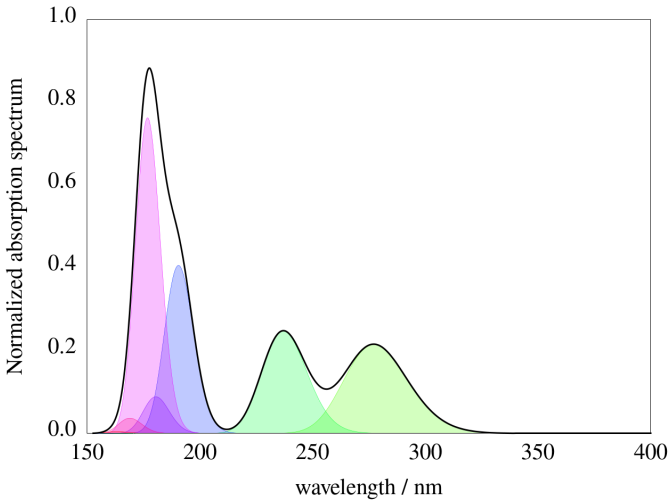

Figure S1: Calculated absorption spectrum at the MRSF-TDDFT/cc-pVDZ level of theory.

2 Comparison between CASPT2 and MRSF-TDDFT

In a previous study,[5] the *meta*-IRC pathway from the FC structure was calculated at the CASPT2 level, whereas in this study, it was calculated at the MRSF-TDDFT level. **Figure S2** shows profiles of potential energies and internal coordinates along *meta*-IRC pathways calculated at the CASPT2 and the MRSF-TDDFT levels. As mentioned in the main text, the MRSF-TDDFT method overestimated excitation energies compared to the CASPT2 method. In the CASPT2-calculated *meta*-IRC pathway, excited-state intramolecular pro-

ton transfer (ESIPT) proceeds smoothly in the S_1 state, followed by a slight energy drop associated with twisting of the hydrated nitro group. Along the ESIPT coordinate, the S_2 state exhibits an energy increase and a barrier. Notably, the MRSF-TDDFT method successfully reproduces those key features observed in the CASPT2 results. Some differences emerge in the latter part of energy profiles. CASPT2 predicts an S_0/S_1 energy crossing at a geometry with a dihedral angle $d_{O3N5C6C7}$ of approximately 30°, whereas the MRSF-TDDFT method places this crossing at around 60°. This difference may arise from the use of single-state CASPT2 method, which can lead to artifacts near crossing regions. In contrast, the MRSF-TDDFT method is capable of describing such regions, including crossings between the ground and first excited states, which standard TD-DFT method typically fail to capture. While a multi-state CASPT2 provides a more balanced description of such crossings, it remains computationally prohibitive for systematic geometry exploration and non-adiabatic molecular dynamics simulations. Therefore, the MRSF-TDDFT represents a promising and practical alternative for these applications.

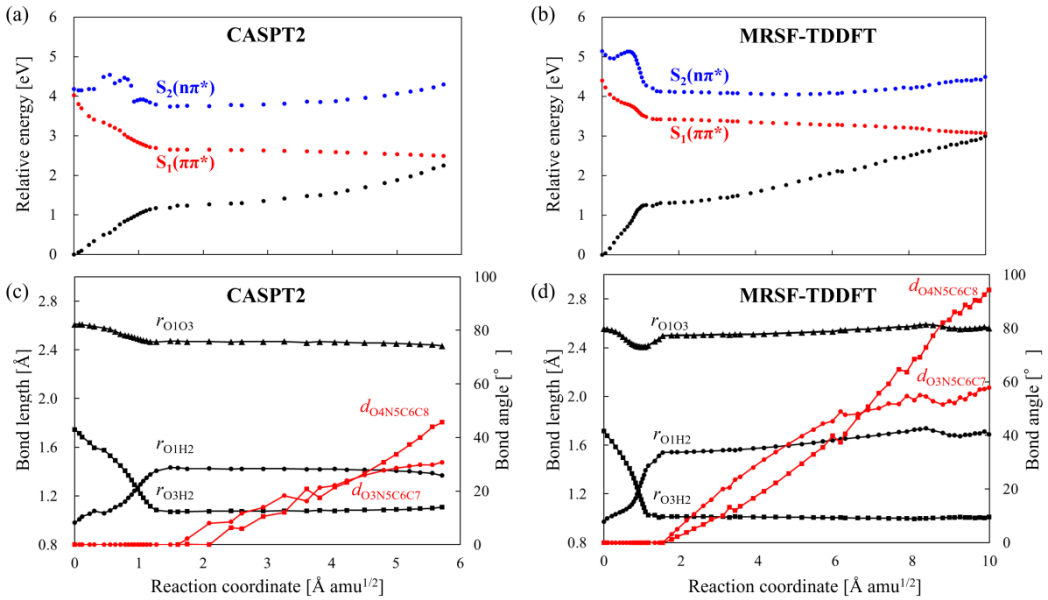

Figure S2: Profiles of potential energies (a: SS-CASPT2, b: MRSF-TDDFT) and internal coordinates (c: SS-CASPT2, d: MRSF-TDDFT) along the *meta*-IRC pathway originating from the Franck-Condon structure in the S_1 state, calculated at each level of theory.

3 The number of surviving trajectories over the course of the simulations

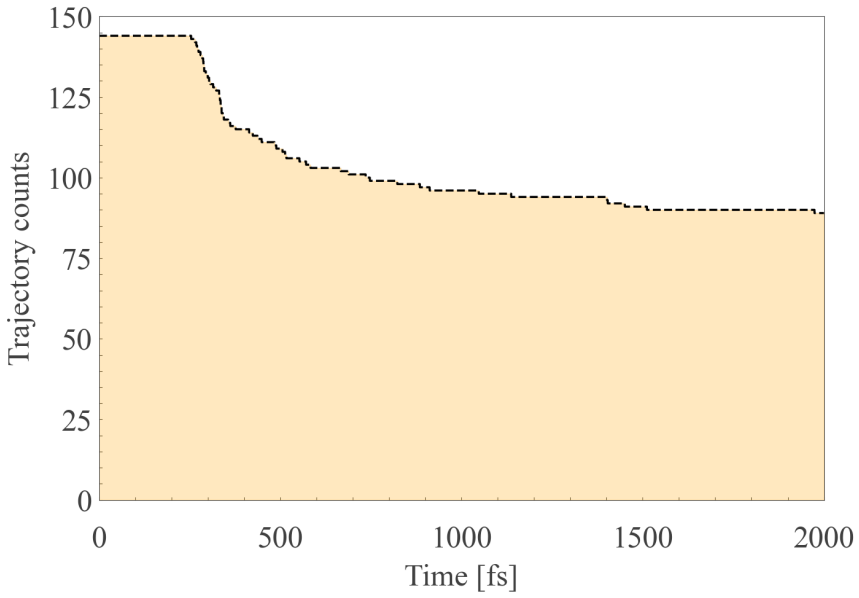

Figure S3: The number of surviving trajectories over the course of the simulations.

Figure S3 shows the number of surviving trajectories over the course of the simulations. A total of 144 trajectories were generated; however, some were terminated before 2 ps due to the convergence issues of the restricted open-shell Kohn-Sham calculations. In total, 49 trajectories were terminated before reaching 2 ps, each after arriving at the S_0 state. Of these 49 trajectories, 48 trajectories were progressing toward S_0-EQ0 (the global minimum corresponding to *o*-NP) following IC from the S_1 state (see Figs. S10-S13), and one trajectory was terminated after reaching the S_0 state via ISC from the T_1 state. (see Fig. S16.) Considering that no trajectory returns to excited-state potential energy surfaces once it hops to the S_0 state, it is reasonable to assume that those terminated trajectories remained and converged in the S_0 state. We have adopted this assumption in the analysis of trajectories that were terminated before 2 ps.

4 Histograms of hopping times between electronic states

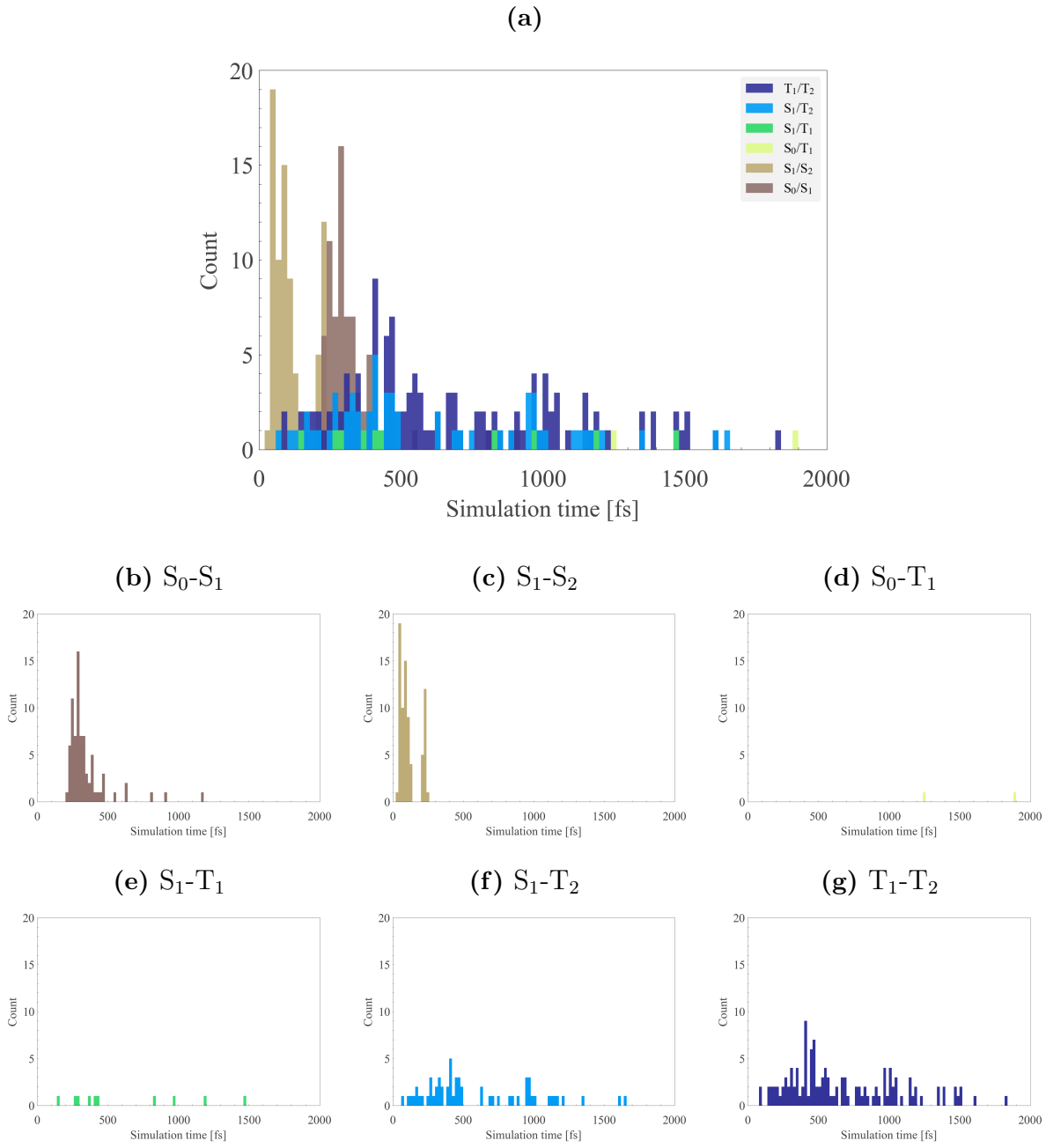

Figure S4: Histograms of hopping times between electronic states.

Figure S4 shows histograms of hopping times between electronic states. Internal conversion (IC) between S_0-S_1 or S_1-S_2 occurs within narrow time ranges, whereas intersystem

crossing (ISC) between S_0-T_1, S_1-T_1, or S_1-T_2 spans wider time ranges.

5 Fitting functions based on first-order kinetics for electronic populations

Population transfer between electronic states was described using first-order kinetics, as represented by the following equation:

$$F_A \underset{k_s}{\overset{k_A}{\rightleftarrows}} \sum_{i \neq A} F_i \tag{1}$$

where F_A represents the population of state A, F_i represents the population of all other states except A, k_A and k_s are the rate constants for the forward and backward reactions, respectively. The decay of the S_1 population was fitted using the following equation:

$$F(t) = (F(t_0) - c)\exp(-\frac{t - t_0}{\tau}) + c, \tag{2}$$

whereas the increase in S_0 and T_1 populations was fitted using the following equation:

$$F(t) = -(1 - F(t_0) - c)\exp(-\frac{t - t_0}{\tau}) + (1 - c) \tag{3}$$

Here, τ and c ($= k_s\tau$) are fitting parameters, and the start time of the fitting (t_0) was set to 200 fs for S_1, 230 fs for S_0, and 100 fs for T_1. Due to the shifted start times, the time constants, which correspond to a lifetime (or a growth time), are evaluated as $\tau + t_0$ in this analysis. **Table S1** shows the obtained time constants for the population transfer between electronic states.

Table S1: Obtained time constants for the population transfer between electronic states, staring time (t_0) and R^2 values.

State	Time constant (fs)	Starting time of fitting (fs)	R^2
S_1	432	200	0.97
S_0	339	230	0.98
T_1	857	100	0.97

6 Time evolution of the absolute value of the dihedral angle

The averaged value of the dihedral angle d_{O3N5C6C7} along the simulation time with a standard deviation are shown in Fig. S5.

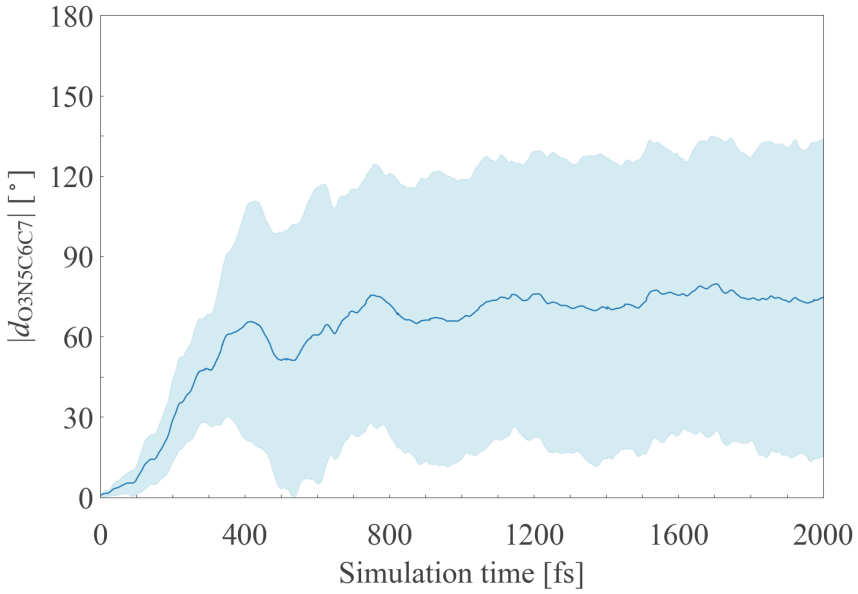

Figure S5: Time evolution of the absolute value of the dihedral angle d_{O3N5C6C7} along the trajectories: the blue curve represents the average. The shaded area represents a standard deviation of all trajectories.

7 Minimum energy conical intersection (MECI) / minimum energy seam of crossing (MESX) structures

MECI/MESX structures were systematically determined using the artificial force induced reaction (AFIR) method, as implemented in the GRRM17 program.[6,7] The gamma parameter for AFIR calculations was set to 150 kJ/mol. Structures initially identified as minima of the AFIR function were subsequently optimized to actual MECI or MESX structures without the application of artificial force. A full list of MECI and MESX structures is provided in **Figures S6** and **S7**, along with their relative energies (in eV) and dihedral angles ($d_{O3N5C6C7}$ and $d_{O4N5C6C8}$).

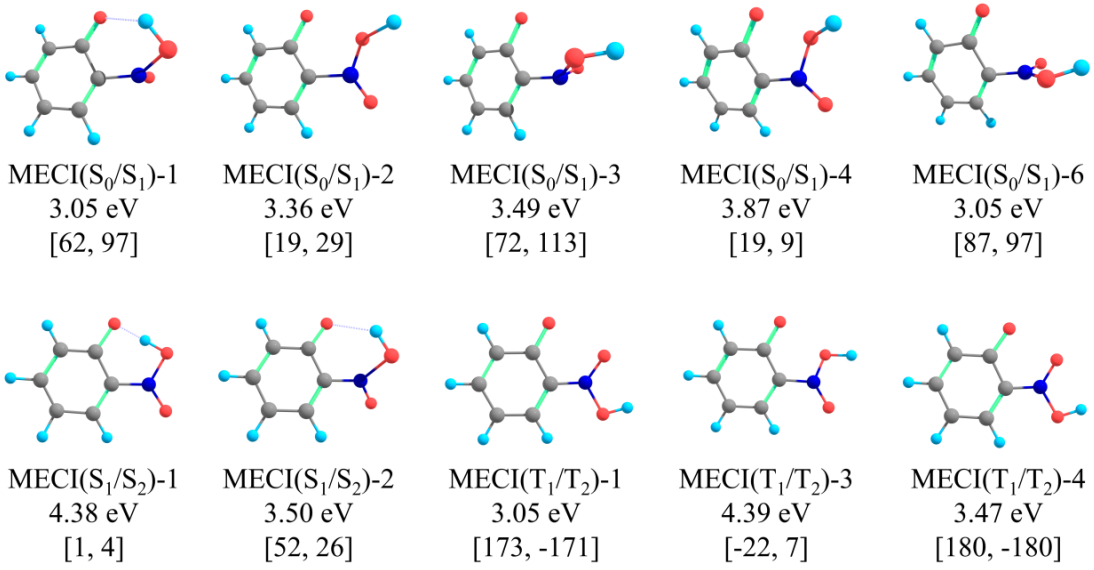

Figure S6: MECI structures between singlet states ($S_0/S_1/S_2$) or triplet states (T_1/T_2). For each MECI structure, the relative energy (in eV) and the dihedral angles ($d_{O3N5C6C7}$ and $d_{O4N5C6C8}$) are also provided.

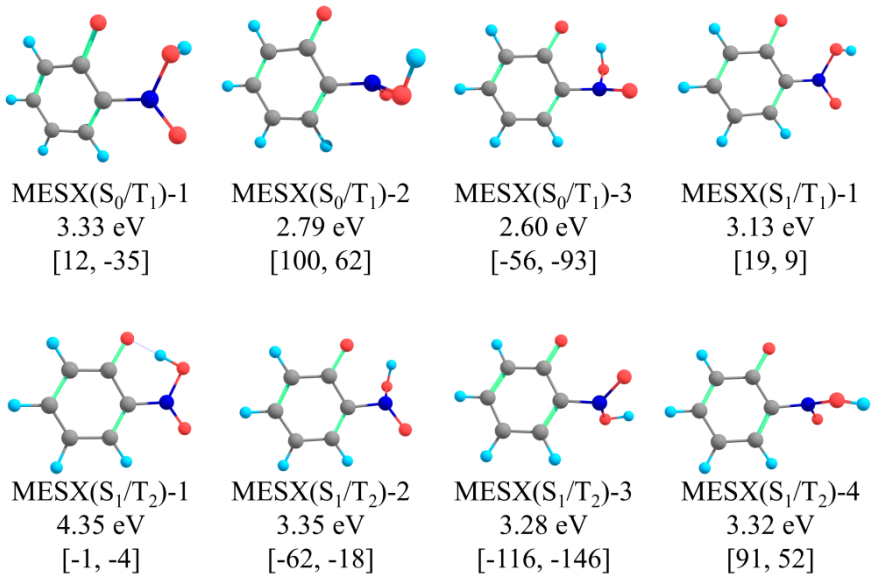

Figure S7: MESX structures between singlet ($S_0/S_1/S_2$) and triplet (T_1/T_2) states. For each MESX structure, the relative energy (in eV) and the dihedral angles ($d_{O3N5C6C7}$ and $d_{O4N5C6C8}$) are also provided.

8 Dynamically accessed MECI/MESX structures with the number of transitions near each structure

To assign each hopping geometry to one of the MECI/MESX structures, the Euclidean distance between them was calculated, and the closest MECI/MESX was assigned. Each molecular structure was rotated by the Kabsch algorithm[8] to align with the reference structure. **Figure S8** summarizes MECI/MESX structures and the number of transitions near each structure. The most frequent IC process between S_1 and S_0 occurred via MECI(S_0/S_1)−1 (70 instances), as anticipated from the *meta*-IRC pathway. Other IC processes between S_1 and S_0 occurred via MECI(S_0/S_1)−3 (once), MECI(S_0/S_1)−4 (6 instances), and MECI(S_0/S_1)−6 (once). IC between S_1 and S_2 occurred via MECI(S_1/S_2)−1 (74 instances) and MECI(S_1/S_2)−2 (two instances), though many trajectories returned via the same MECI. ISC between S_1 and T_2 occurred via MESX(S_1/T_2)−1 (23 instances), MESX(S_1/T_2)−2 (31 instances), and MESX(S_1/T_2)−4 (6 instances). ISC between S_1 and

T_1 via MESX(S_1/T_1)−1 occurred in only 10 transitions. Thus, the increasing T_1 population is primarily attributed to IC between T_1 and T_2 via MECI(T_1/T_2)−3, which accounted for 124 transitions. ISC between S_0 and T_1 occurred via MESX(S_0/T_1)−1 (once) and MESX(S_0/T_1)−2 (once).

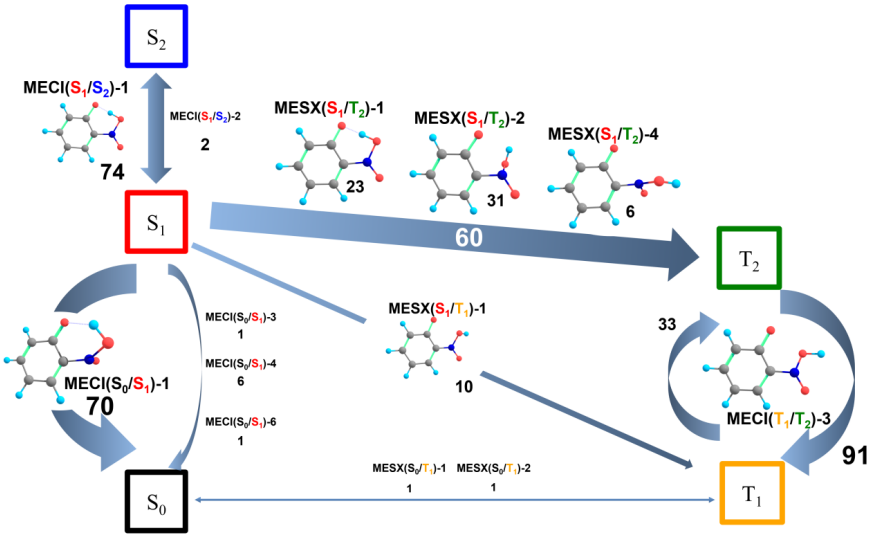

Figure S8: Dynamically accessed MECI/MESX structures with number of transitions near each structure.

9 Trajectory classification by Reaction Space Projector (ReSPer)[1–3] analysis

The 144 trajectories were categorized based on their hopping time from the S_1 state and the results of the ReSPer analysis, providing a comprehensive view of the various decay pathways observed in the simulations. Among these, 29 trajectories (**Fig. S9**) underwent IC via MECI(S_0/S_1)−1 within 660 fs (= 433 + 227 fs), which represents the upper bound of the time constant for the single-exponential rising signal observed in the experiment,[5] leading to S_0-EQ3 (*aci*-NP). Similarly, 34 trajectories (**Fig. S10**) followed a comparable IC pathway via MECI(S_0/S_1)−1 within 660 fs, but instead, proceeded to S_0-EQ0 (*o*-NP). Meanwhile, seven trajectories (**Fig. S11**) underwent IC via a different MECI, distinct from MECI(S_0/S_1)−1. Additionally, five trajectories (**Fig. S12**) initially underwent IC via MECI(S_0/S_1)−1, but instead of settling into a stable equilibrium, they ultimately diverged on the S_0 state. Furthermore, three trajectories (**Fig. S13**) hopped to the S_0 state via IC after 660 fs, suggesting an alternative, slower decay pathway. Regarding ISC processes, 42 trajectories (**Fig. S14**) hopped to the triplet state within 660 fs and remained there until 2 ps, while 22 trajectories (**Fig. S15**) underwent ISC to the triplet state after 660 fs, also persisting in the triplet state for the remainder of the simulation. Lastly, two trajectories (**Fig. S16**) exhibited a rare ISC event from the T_1 to the S_0 state. These classifications provide a detailed picture of the competitive non-adiabatic pathways in photoexcited *o*-NP, highlighting the dominance of ultrafast IC and ISC processes and explaining the observed ultrafast-decaying and long-lived excited-state signals in experimental studies.

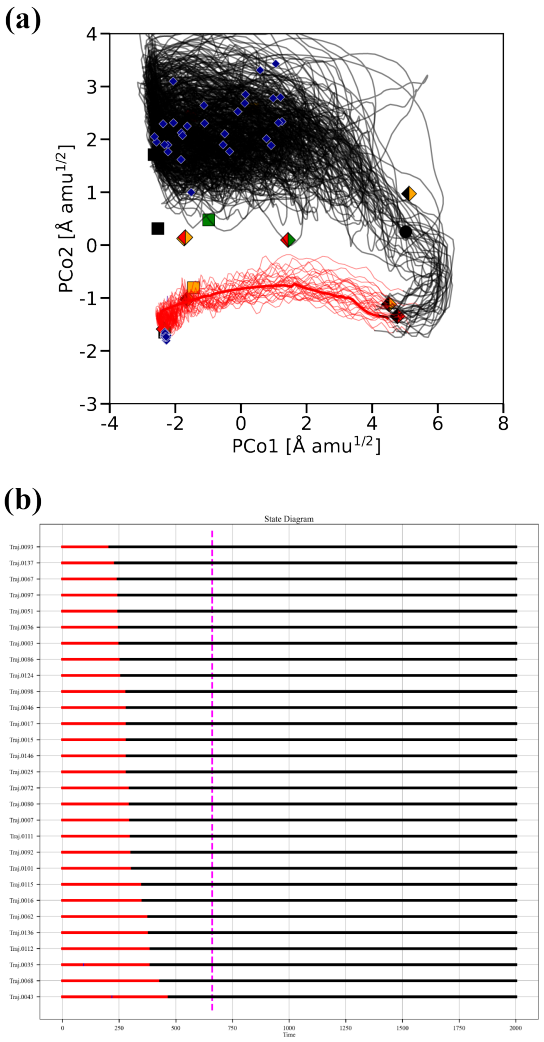

Figure S9: (a) Projected trajectories onto the two-dimensional reaction space from Fig. 4a in the main text. A total of 29 trajectories undergo IC via MECI(S_0/S_1)−1 within 660 fs, which represents the upper bound for the time constant for the single-exponential rising signal observed in experiments, subsequently proceeding to S_0-EQ3 (*aci*-NP). (b) State diagram of the 29 trajectories, where the electronic states S_0 and S_1 are represented in black and red, respectively. Gray regions indicate missing trajectory data due to convergence issues in electronic structure calculations. The pink dotted line marks the upper bound of 660 fs.

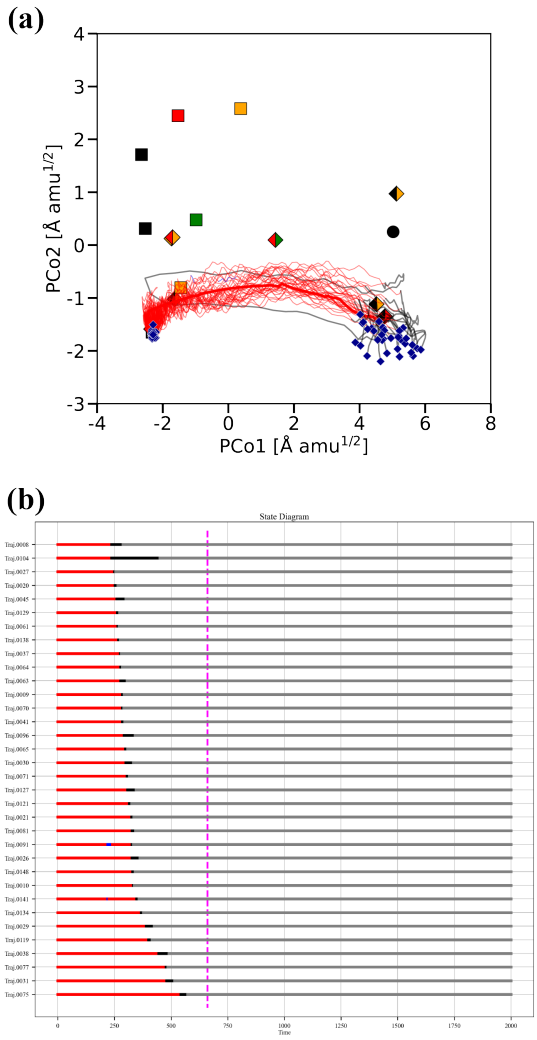

Figure S10: (a) Projected trajectories onto the two-dimensional reaction space from Fig. 4a in the main text. A total of 34 trajectories undergo IC via MECI(S_0/S_1)−1 within 660 fs, subsequently proceeding to S_0-EQ0 (*o*-NP). (b) State diagram of the 34 trajectories, where the electronic states S_0, S_1, and S_2 are represented in black, red, and blue, respectively. Gray regions indicate missing trajectory data due to convergence issues in electronic structure calculations. The pink dotted line marks the upper bound of 660 fs.

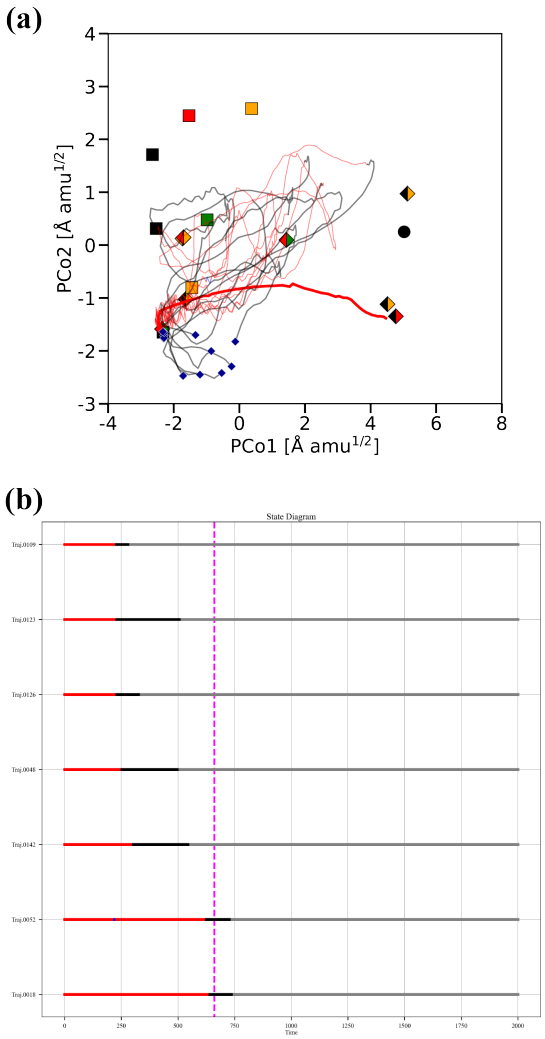

Figure S11: (a) Projected trajectories onto the two-dimensional reaction space from Fig. 4a in the main text. A total of seven trajectories undergo IC via an MECI distinct from MECI(S_0/S_1)−1, ultimately proceeding to the S_0-EQ0 (*o*-NP) region. (b) State diagram of the seven trajectories, where the electronic states S_0, S_1, and S_2 are represented in black, red, and blue, respectively. Gray regions indicate missing trajectory data due to convergence issues in electronic structure calculations. The pink dotted line marks the upper bound of 660 fs.

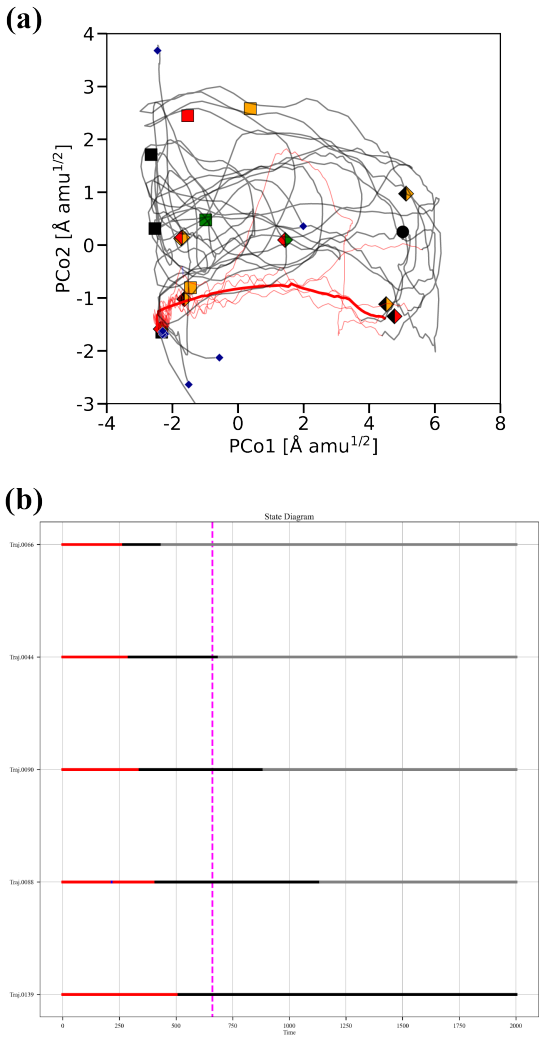

Figure S12: (a) Projected trajectories onto the two-dimensional reaction space from Fig. 4a in the main text. A total of five trajectories undergo IC via MECI(S_0/S_1)−1 but ultimately diverge on the S_0 state instead of settling into a stable equilibrium structure. (b) State diagram of the five trajectories, where the electronic states S_0, S_1, and S_2 are represented in black, red, and blue, respectively. Gray regions indicate missing trajectory data due to convergence issues in electronic structure calculations. The pink dotted line marks the upper bound of 660 fs.

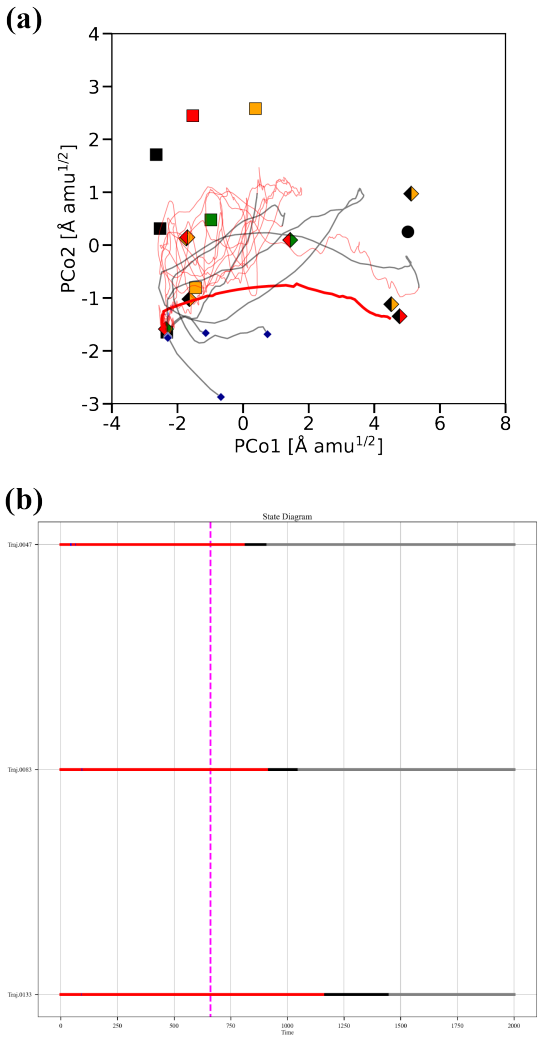

Figure S13: (a) Projected trajectories onto the two-dimensional reaction space from Fig. 4a in the main text. A total of three trajectories undergo IC to the S_0 state at a time later than 660 fs. (b) State diagram of the three trajectories, where the electronic states S_0, and S_1, are represented in black, and red, respectively. Gray regions indicate missing trajectory data due to convergence issues in electronic structure calculations. The pink dotted line marks the upper bound of 660 fs.

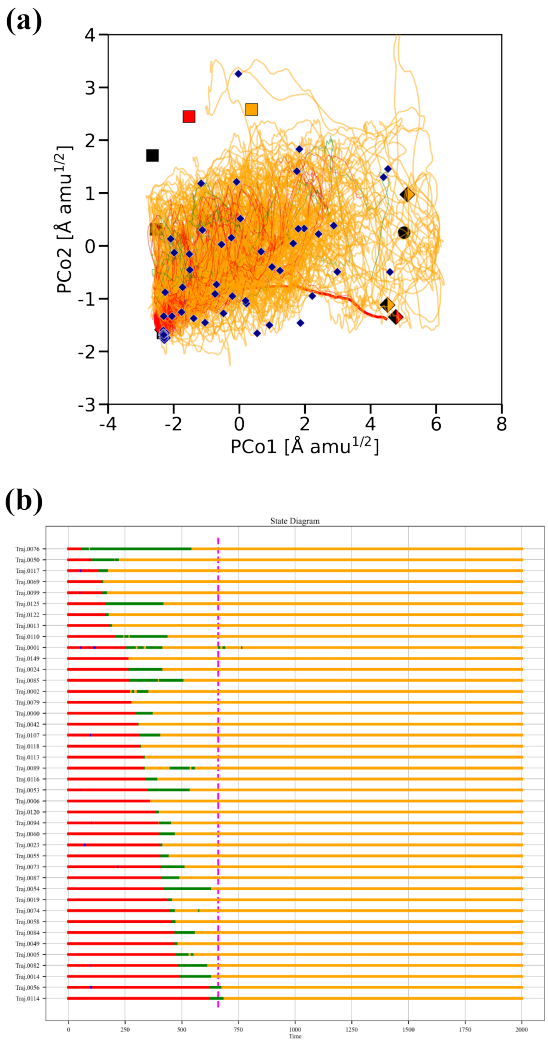

Figure S14: (a) Projected trajectories onto the two-dimensional reaction space from Fig. 4a in the main text. A total of 42 trajectories undergo ISC to the triplet state within 660 fs and subsequently remain in the triplet state until 2 ps. (b) State diagram of the 42 trajectories, where the electronic states S_1, S_2, T_1, and T_2 are represented in red, blue, orange, and green, respectively. The pink dotted line marks the upper bound of 660 fs.

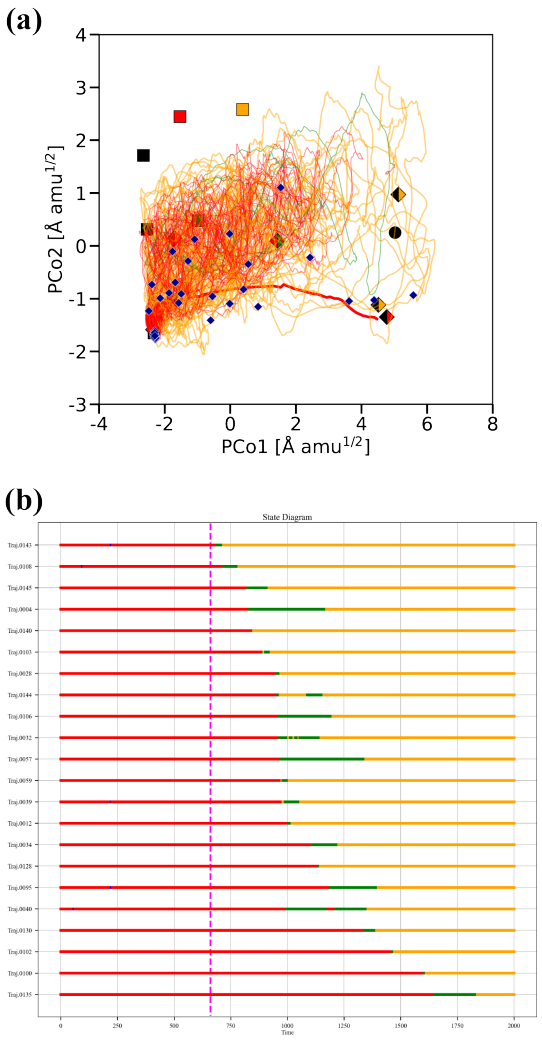

Figure S15: (a) Projected trajectories onto the two-dimensional reaction space from Fig. 4a in the main text. A total of 22 trajectories undergo ISC to the triplet state after 660 fs and subsequently remain in the triplet state until 2 ps. (b) State diagram of the 22 trajectories, where the electronic states S_1, S_2, T_1, and T_2, are represented in red, blue, orange, and green, respectively. The pink dotted line marks the upper bound of 660 fs.

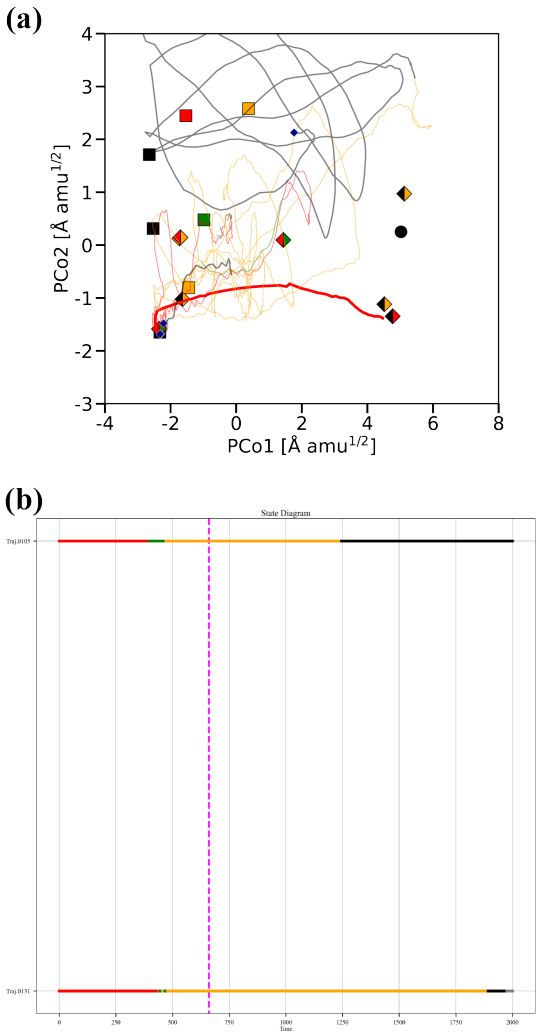

Figure S16: (a) Projected trajectories onto the two-dimensional reaction space from Fig. 4a in the main text. A total of two trajectories undergo ISC from the T_1 to the S_0 state. (b) State diagram of two trajectories, where the electronic states S_0, S_1, T_1, and T_2, are represented in black, red, orange, and green, respectively. Gray regions indicate missing trajectory data due to convergence issues in electronic structure calculations. The pink dotted line marks the upper bound of 660 fs.

References

(1) Tsutsumi, T.; Ono, Y.; Arai, Z.; Taketsugu, T. Visualization of the intrinsic reaction coordinate and global reaction route map by classical multidimensional scaling. *Journal of Chemical Theory and Computation* **2018**, *14*, 4263–4270.

(2) Tsutsumi, T.; Ono, Y.; Arai, Z.; Taketsugu, T. Visualization of the dynamics effect: projection of on-the-fly trajectories to the subspace spanned by the static reaction path network. *Journal of chemical theory and computation* **2020**, *16*, 4029–4037.

(3) Tsutsumi, T.; Ono, Y.; Taketsugu, T. Visualization of reaction route map and dynamical trajectory in reduced dimension. *Chemical communications* **2021**, *57*, 11734–11750.

(4) Ernst, H. A.; Wolf, T. J.; Schalk, O.; González-García, N.; Boguslavskiy, A. E.; Stolow, A.; Olzmann, M.; Unterreiner, A.-N. Ultrafast dynamics of *o*-nitrophenol: An experimental and theoretical study. *The Journal of Physical Chemistry A* **2015**, *119*, 9225–9235.

(5) Nitta, Y.; Schalk, O.; Igarashi, H.; Wada, S.; Tsutsumi, T.; Saita, K.; Taketsugu, T.; Sekikawa, T. Real-time probing of an atmospheric photochemical reaction by ultrashort extreme ultraviolet pulses: Nitrous acid release from o-nitrophenol. *The Journal of Physical Chemistry Letters* **2021**, *12*, 674–679.

(6) Maeda, S.; Ohno, K.; Morokuma, K. Systematic exploration of the mechanism of chemical reactions: the global reaction route mapping (GRRM) strategy using the ADDF and AFIR methods. *Physical Chemistry Chemical Physics* **2013**, *15*, 3683.

(7) Maeda, S.; Harabuchi, Y.; Sumiya, Y.; Takagi, M.; Suzuki, K.; Hatanaka, M.; Osada, Y.; Taketsugu, T.; Morokuma, K.; Ohno, K. GRRM17. `http://iqce.jp/GRRM/index_e.shtml`.

(8) Kabsch, W. A solution for the best rotation to relate two sets of vectors. *Foundations of Crystallography* **1976**, *32*, 922–923.